5-24-2023

Experiments and Data Analysis for Modulated Phase Gratings in X-rays

Sydney B. Carr
Louisiana State University and Agricultural and Mechanical College

EXPERIMENTS AND DATA ANALYSIS FOR MODULATED PHASE GRATINGS IN X-RAYS

A Thesis

Submitted to the Graduate Faculty of the
Louisiana State University and
Agricultural and Mechanical College
in partial fulfillment of the
requirements for the degree of
Master of Science

in

The Department of Physics and Astronomy

by
Sydney Briann Carr
B.S., Houston Baptist University, 2020
August 2023

This work is dedicated to my parents,
Angel and Brian Carr, who continuously
loved and supported the dreams of
their "little mad scientist."

“Education is the most powerful
weapon which you can
use to change the world.”
-Nelson Mandela

Acknowledgments

I would like to first thank my research advisor, Dr. Joyoni Dey, for her unconditional support and consistent guidance throughout the duration of this work. She never once doubted my abilities as a professional and encouraged me to be my best self. Without her mentorship, I wouldn't be where I am today. I would also like to thank my research advisory committee – Dr. Kristina Launey and Dr. Garrett Pitcher, for their time and feedback. I also want to thank Dr. Kyungmin Ham and Dr. Les Butler for offering their years of experience in experimental x-ray interferometry and tomography, helping to teach and guide me while operating a multitude of devices and x-ray machinery.

I would like to thank the entire faculty and staff of the medical and health physics program for their exquisite teaching abilities and mentorship throughout graduate school. To all the newly acquired mentors, friends and "family" I have made through the National Society of Black Physicists for their constant reassurance, encouragement and help with navigating through academia as a minority and student of color. A special thank you to my fellow NSBP councilman – Elon Price, Tracy Edwards, Farrah Simpson, Allen Pierre-Louis, Morgan Cole, Carlton Smith, Preston Ohanuka, Refilwe Tanah Bua, and Samantha O'Sullivan, for their love, warm familiarity and for being so uplifting for me throughout this work.

I would like to thank my student peers for creating such a memorable and worthwhile experience for me in my graduate studies, but specially to Nousha Afshari and Lacey Medlock for their much-needed friendship and support. A sincere thank you to Ivan Hidrovo, who ushered me into the world of x-ray interferometry as both a student colleague and a friend. To my entire family, my mother and father, and to my sister, Morgan Carr, for the encouragement and support throughout my entire life. A purposeful thank you to my late grandmother, Shirley Curette, for

her unconditional love and support, as well as being my inspiration to pursue Medical Physics due to her long fight with cancer. A special thank you to my sister, for the many memories of testing and challenging my knowledge as a child, ultimately opening a door and unleashing the determination within me to advance in academia and chase my dreams to become a physicist.

Table of Contents

List of Figures

Nomenclature

SAXS	Small-angle X-ray Scattering
TLXI	Talbot-Lau X-ray Interferometry
G0	Source Grating
G1	Phase Grating
G2	Absorption Grating
MPG	Modulated Phase Grating
TRMPG	Triangular Modulated Phase Grating
MPG7	Rectangular Modulated Phase Grating
CAMD	Center for Advanced Microstructures and Devices
PNNL	Pacific Northwest National Laboratory
PBRC	Pennington Biomedical Research Center
G0-MPG	Source Grating to Modulated Phase Grating Distance
FFT	Fourier Transform
IFFT	Inverse Fourier Transform

Abstract

Purpose: Modulated Phase Grating (MPG) interferometry has been shown in theory and simulations to produce observable fringes on a clinical detector without requiring fluence absorbing analyzer. In this work, we will experimentally show that the MPG X-ray system produces observable fringes and multi-modal X-ray images.

Motivation: Nearly 1 in 8 women in the US will develop invasive breast cancer in their lifetime, accounting for approximately 40,000 deaths each year [1-2]. In order to pursue the best treatment option available, cancer itself must be adequately imaged and staged, based on size and level of metastasis, on the order of Stage I-IV. Currently, the most used imaging modality for breast cancer screening is mammography. Along with the traditional x-ray absorption images from mammography, the effects created from scattered x-rays at small angles (SAXS) can be utilized in the creation of multiple modalities generated from the same scan. Incorporating phase-shift and SAXS images in addition to the traditional attenuation images allow for an overall increase in contrast and the better detection of micro-calcifications, a risk factor for breast cancer. The advantage of MPG over prevalent Talbot Lau interferometry system is that MPG does not require fluence absorbing analyzer and therefore dose to patient can be maintained similar to conventional X-ray. Thus, MPG *can be used* for breast cancer screening mammography.

Methods: Experiments were performed with 8 keV test MPG gratings as well as two 25 keV MPG gratings, all manufactured by Microworks, GmbH. At LSU's CAMD, the 8keV beamline was used to test the preliminary8 keV grating. We implemented both a deconvolution and linear optimization estimation method to remove the G0 grating effects seen in the detected fringe patterns. Experiments at Pacific Northwest National Lab (PNNL) were done using 25 keV design energy gratings placed in a X-ray tomography machine to test various constraints and

limits of the proposed MPG system, leading us to the Pennington Biomedical Research Center (PBRC, LSU) experiments. Here, the Keck x-ray tomography machine (at PBRC) was used to measure the visibility at various set-up distances and imaged various samples (anchovy, chicken bone, seeds).

Results: For the CAMD experiments, we successfully removed the G0 effects to get similar results from the deconvolution and linear optimization methods. The PNNL experiments showed the limit of larger detector pixel size for MPG system set-up. The PBRC experiments showed that we were again able to view fringe patterns of MPG, calculate visibility and also see attenuation and small angle X-ray scattering images of samples.

Conclusion: The CAMD experiments yielded recovered fringe patterns with period lengths of $208\mu m - 264\mu m$, roughly twice the period of the MPG used. At the PBRC, the visibility calculations illustrated that the farther the MPG is from the detector, the more the visibility increased. We obtained attenuation, differential phase and small angle x-ray scattering images of samples. The triangular MPG also yielded better results than the rectangular MPG used.

Chapter 1. Introduction

1.1. Motivation

Nearly 1 in 8 women in the United States will develop invasive breast cancer within their lifetime, accounting for approximately 40,000 deaths each year [1-2]. In order to pursue potential treatment options for a breast cancer patient, the cancer itself must be detected, diagnosed and staged, based on size, possible metastasis and possible nodal involvement on the order of Stage I-IV [30]. The 5-year survival rate of breast cancer patients improves dramatically from 22% when detected in Stage IV to 90% if detected in earlier stages [3]. Thus, screening is a vital key to reducing the death rate resulting from breast cancer [4].

Currently, the most used modality for the screening and imaging of breast cancer is mammography with an estimated 40 million women in the United States that undergo mammography screening each year. In order to obtain a sufficient diagnosis, mammogram systems must possess a very high spatial resolution that can distinguish the morphological features of normal soft tissue from malignant, or cancerous, tissue that can often present itself as fine microcalcifications [28].

Furthermore, when screening for diseases, the effectiveness of a modality can be described in terms of sensitivity, the ability of a test to correctly classify an individual as “diseased,” and specificity, the ability of a test to classify an individual as “disease-free” [27]. In the United States, mammography currently has a 92% sensitivity and 84-92% specificity [5]. The 8-16% rate of false positives that result from this screening often causes unnecessary stress for the patients and costs around $7.9 billion per year [6-7] in follow-up imaging and tissue biopsies, becoming a significant contributor to health-care costs in the USA [6]. By reducing false positive rates by even 1%, we can create a large impact by saving billions of dollars annually in unnecessary, additive health-care costs.

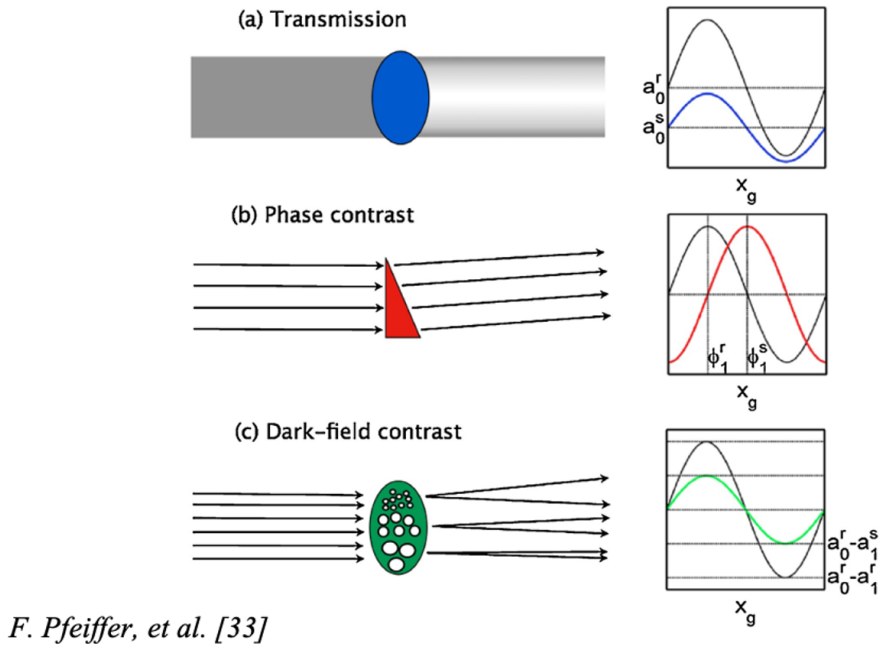

Figure 1.1. Schematic illustrating (A) transmission, (B) phase contrast, (C) dark-field contrast image formation by x-rays.

Traditional mammography images used for the screening of breast cancer are formed due to the interaction of the x-ray beam with the patient's tissue as it transverses through it [31]. The varying in x-ray beam intensity is directly dependent on the varying tissue types, its composition and its attenuation properties [31]. This phenomenon is illustrated in Figure 1.11(A) below. The denser the tissue, the more the x-ray beam will be absorbed, or attenuated, by it. The more the x-ray beam is absorbed in an area, the "whiter" this area will be in the resulting x-ray image [31]. The varied attenuation properties of different tissues allow for contrast in an absorption x-ray image that aids in distinguishing different structures [31].

Along with the absorption of x-rays, the x-ray beam has diffraction and refraction effects [22]. These effects can be seen as a phase-shift in the resultant x-ray wave. Due to the differences of refractive properties of different tissues, x-ray images can be produced using this

additive property for contrast [22]. This method of imaging, deemed differential-phase contrast imaging, can increase the soft tissue contrast of the absorption imaging method in mammography. This type of image formation is illustrated in Figure 1.11(B) below. When the x-ray beam is scattered, it can also be elastically scattered at very small angles that results in the reduction of its intensity radially in a cone shape after interacting with structures much larger than the x-ray beam's wavelength [22]. This type of interaction, deemed small-angle x-ray scattering or SAXS, produces contrast in an x-ray image that allows for the detection of nano-scaled and micro-scaled structures in a sample [22], as shown as Figure 1.11(C) below. This is crucial when trying to identify and distinguish malignant microcalcifications in a patient's breast tissue. Applying this phase-contrast imaging method would also allow for a non-invasive method of classifying microcalcifications as either type I (typically benign) and type II (typically malignant) based on their different chemical composition [32].

Phase contrast x-ray interferometric imaging provides not only attenuation contrast images (like conventional mammography), but also differential phase-shift and small angle scatter (SAXS) or dark-field images, all in one single exposure [22]. The prevalent Talbot-Lau X-ray interferometry (TLXI) system [8-11],., has shown the potential to improve radiographic accuracy in detecting tumors [12-14] and in classifying micro-calcifications [15]. This provides a potential for improving both detection and diagnosis [16, 17] as well as specificity. However, multi-contrast modalities of the TLXI system comes at the cost of increased radiation dose to the patient, which inhibits it from being used in clinical screening (due to dose regulation for mammograms).

The TLXI system has both a source grating, G0, and then a phase grating, G1 that is semi-transparent to x-rays, to slit the beam locally causing interference patterns to form at the

detector. However, they are only between 4 or5 microns from peak to peak. Therefore, an absorption or analyzer grating, G2, is needed between object and detector to act like a "mask," creating larger moiré patterns 150-300 microns. This is then visible on a clinical, flat panel detector with a pixel-size of 50 microns. Unfortunately, the G2 grating will absorb around half of the x-rays. Thus, in order to maintain same fluence of x-rays at the detector, the fluence of the x-rays will need to be doubled, which in turn will increase the dose to object. This inhibits the TLXI system from being directly used in clinical screening mammography where the dose is regulated to be between 3 to 4 mGy in the United States.

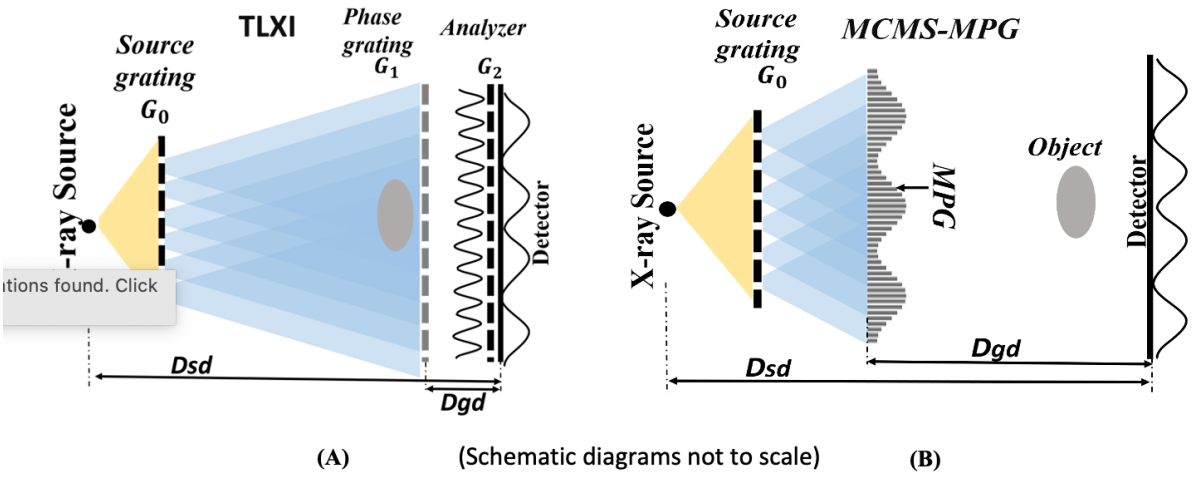

Courtesy of Jingzhu Xu.

Figure 1.2. (A) Schematic of current TLXI system set-up and (B) our proposed MCMS-MPG system set-up.

Dr. Joyoni Dey and our research group as a collective has proposed multi-contrast mammography system with modulated phase gratings, or MPG system, uses a structured phase grating with rectangular or triangular modulation which creates large enough fringe patterns on the detector without requiring an analyzer grating, or G2 grating, in which our group has already shown through simulations [18-20]. No analyzer grating means no need to double the fluence of x-rays, consequently decreasing the dose to the object, or essentially the patient. Hence, this can

be used in screening mammography.

A G0 grating is still needed in the system set-up for creating a coherent source for the MPG, or G1 grating, but there is ultimately a loss of visibility if the G0 pitch is incorrect. This "G0 effect" can be thought of as a linear kernel and even further approximated as a convolution of the individual fringe patterns of the MPG and G0 gratings. However, there is also some deconvolution due to slit opening of the G0 because the slit is not an exact point source, but a line source. This G0 effect is illustrated in the schematic below in Figure 1.2.

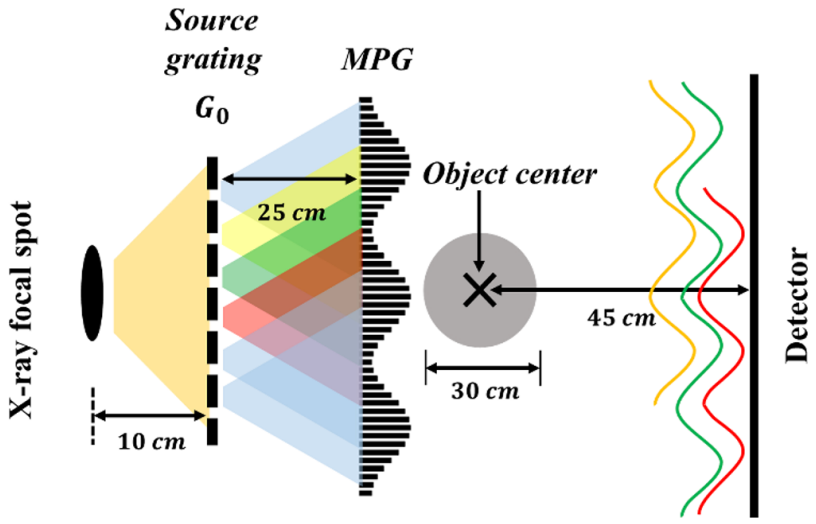

Courtesy of Jingzhu Xu.

Figure 1.3. Illustration of the G0 Effect.

1.2. Purpose

Our group's prior publications have shown MPG in theory and simulations [22, 23]. We wish to experimentally prove that our proposed MCMS-MPG system produces observable fringes and good quality multi-modal images.

Chapter 2. Three Sets of Experiments

2.1. Center for Microstructures and Devices - CAMD

For the first set of experiments, data sets were collected at LSU's Center for Microstructures and Devices (CAMD) in Baton Rouge, Louisiana using a beamline from the synchrotron and a low-quality modulated-phase grating, or MPG. This specific MPG was effectively tuned for an 8 keV beam. For the G0, or source grating, just an available G0 grating was used at the time. However, this did not affect the outcome of our experiments due to the G0 effect which will be expanded upon later within this paper.

2.2. Pacific Northwest National Laboratory – PNNL

Experiments were next performed at Pacific Northwest National Laboratory (PNNL) in Richland, Washington using an x-ray tomography system. The data sets collected and analyzed at PNNL revealed that a small source was excellent for our purpose, however, the detector was rather large with each pixel size equal to192 μm. This caused issues when trying to observe the small fringe patterns hitting the detector. In order to both fulfill a desired higher spatial resolution and to be able to have adequate visibility of the fringe patterns, a small source in addition of a small detector pixel is required for our proposed system set-up. We used the results from these trials to further investigate now in the correct direction.

2.3. Pennington Biomedical Research Center – PBRC

When returning to Baton Rouge, experiments were done at Pennington Biomedical Research Center (PBRC) using an x-ray tomography system. This system had both a small source and a small detector pixel size of 75 μm which served as the ideal conditions we needed for our proposed MCMS-MPG system set-up.

Chapter 3. Specific Aims

In this work, the details surrounding the methods used behind the CAMD and PBRC experiments and data analysis will be thoroughly explained. This being because the experiments at PNNL served mainly as a directional pivot in the research when testing and evaluating both the conditions needed and the limits for our proposed MCMS-MPG system.

3.1. Experiment at CAMD & Data Analysis

3.1.1. Experimental – Beamline Port 5A: MPW-Biomed-Tomo

The experiments were conducted using an 8 keV beamline as the source at LSU CAMD specifically using the beamline detailed as Port 5A: MPW-Biomed-Tomo. In Figure 3.1(c), the source is seen at the top of the image, followed by the G0, or source grating, then followed by the G1 grating. The G1 grating seen in Figure 3.1(c), is the rectangular modulated phase grating with a phase modulation, height 1 and height 2, are such that phase shifts are 0.74π and 0.93π at 8 keV, illustrated in the schematic in Figure 3.1(d). The detector was a scintillator and a high-resolution sCMOS camera (PCO.edge 4.2 LT) with a 2048x2048 full frame with each pixel size equal to 6.5μm [23]. When detecting the x-rays, the scintillator would convert the x-ray energy into visible light that could then be picked up by the camera [23].

The schematic in Figure 3.1(d) illustrates the experimental set-up in terms of distances and dimensions, although not to scale. The G0 to detector distance was 48cm and kept constant between exposures with a varying MPG to detector distance of 2cm, 10cm and 15cm. The pitch of the grating is represented by P and the grating's period represented by W, which in this case is equivalent to 120 μm. The accuracy of the height 1 and height 2 were verified at CAMD through measurements under a microscope before any experiments were initiated.

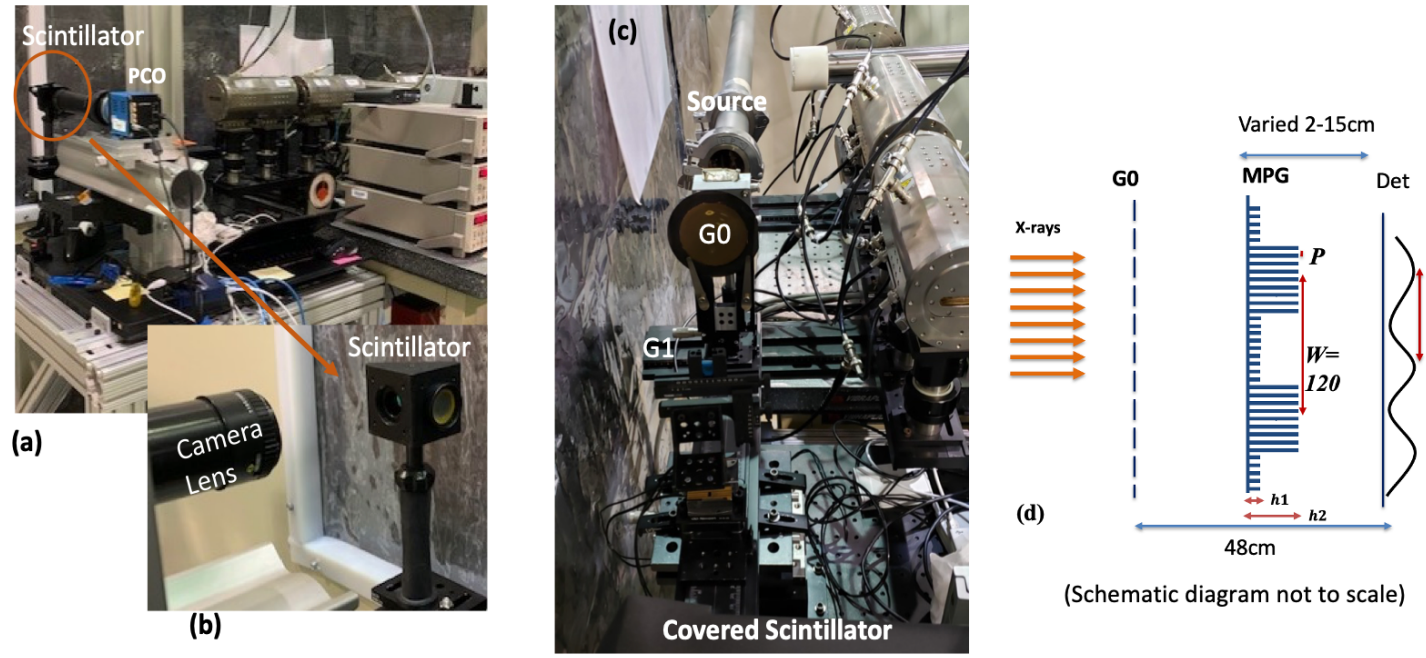

I. Hidrovo, S. Carr, et al. [23]

Figure 3.1. (A-B) Camera and scintillator set-up. (C) Source, G0 and G1 placement in relation to covered camera-scintillator set-up (D) Schematic of CAMD set-up.

3.1.2. Data Analysis – Deconvolution

Considering the G0 effect, we collected x-ray images with the G0 grating alone and images with the MPG+G0 grating combination. In order to achieve getting the effect of the MPG alone, we needed to perform a method of deconvolution between the G0 and MPG+G0 signals, doing so for all three cases of MPG to detector distances of 2cm, 10cm and 15cm while utilizing MATLAB software.

To perform a deconvolution, we first normalized the relative attenuation between the MPG+G0 and the G0 alone plots (i.e., making them have the same average signal).

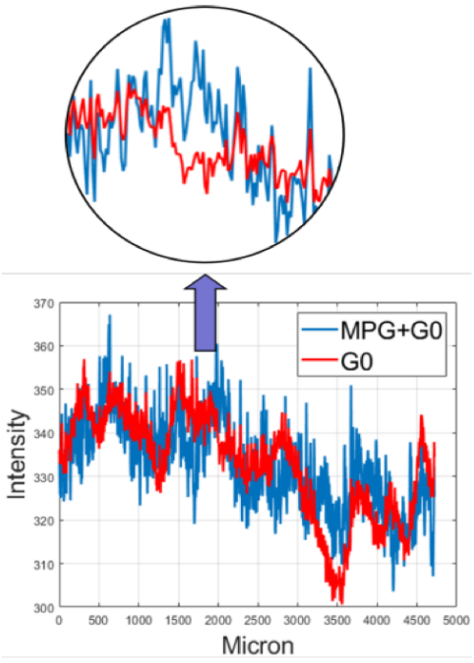

I. Hidrovo, S. Carr, et al. [23]

Figure 3.2. Example of normalization step for MPG-detector distance equal to 2cm.

In Figure 3.2 below, the result of this step performed is shown for the 2cm case (MPG to detector distance). The recovered MPG+G0 signal is shown in blue and the G0 alone signal is shown in red. The two signals can be distinguished right away because the oscillation amplitude is higher for the blue MPG+G0 signal than the red G0 signal [23].

In order to extract the MPG only signal, we must do so in the fourier domain. Therefore, next we took the fourier transform (FFT) of both the G0 and MPG+G0 signals followed by taking the ratio of the two respectively, as shown below for clarification:

$$\frac{FFT(MPG + G0)}{FFT(G0)} \qquad (1)$$

As a result, a pair of clear, dominant frequency spikes were revealed, as seen in Figure 3.3 below for the 2cm case. By taking the inverse fourier transform (IFFT) of this right away, we ultimately now have deconvolved the MPG+G0 and G0 signals, however, the recovered MPG only pattern is very noisy, as seen in Figure 3.4 below.

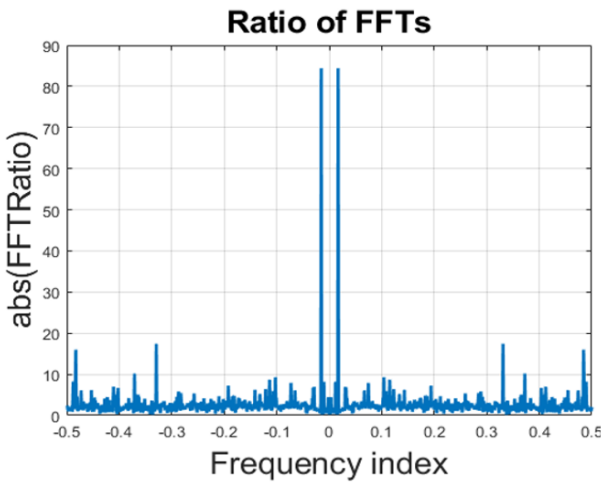

I. Hidrovo, S. Carr, et, al. [23]

Figure 3.3. Ratio of FFT(MPG+G0) by FFT(G0) for 2cm case.

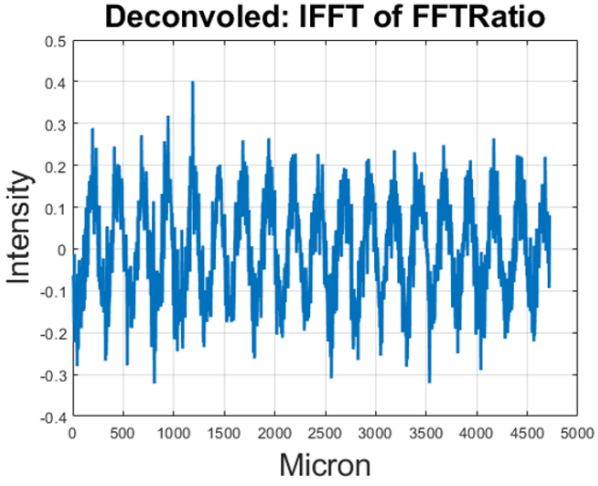

I. Hidrovo, S. Carr, et, al. [23]

Figure 3.4. IFFT of the ratio of FFT(MPG+G0) by FFT(G0) for 2cm.

In order to attain a recovered MPG only signal with reduced noise, we kept only the dominant harmonic peak-pair seen in Figure 3.5, again for the 2cm case as a visual example, isolating just them before performing an inverse fourier transform.

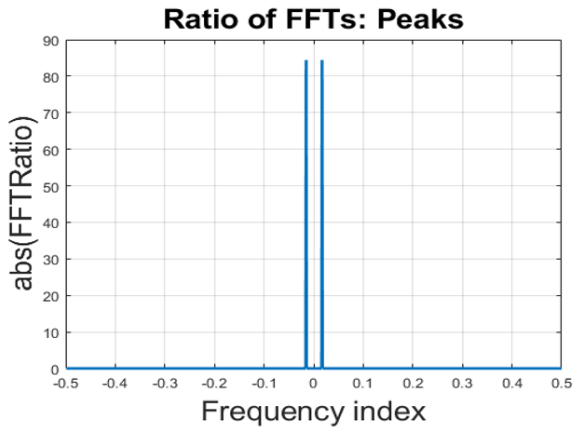

I. Hidrovo, S. Carr, et, al. [23]

Figure 3.5. Extracted dominant frequency peaks from FFT ratio for 2cm.

3.1.3. Data Analysis – Linear Optimization Estimation

For the case where the G0 to MPG distance was 10cm, we applied a linear optimization estimation method, minimizing the sum-squared error. We did so because the deconvolution method is more constricting than the method of linear optimization [23]. The G0 only and MPG+G0 data can be related by Eq. (2) below, which is more general than the convolution assumption from earlier:

$$\check{s} = a_1 x_1 + \cdots + a_n x_n \qquad (2)$$

Under the assumption that both data sets are related via Eq. (1), the MPG+G0 combination data, denoted $\check{s}$, and the G0 only fringe pattern data, denoted as x. Minimization of the sum-squared error allows us to find the intensity effect of MPG only, given by a vector A

with coefficients a_i, shown in Eq. (3) [23]:

$$A = R_0 R^{-1} \tag{3}$$

Here, R is the $n \times n$ autocorrelation matrix for the *x* variable and the vector R_0 is the cross-correlation vector between *x* and $\check{s}$ [23]. Now with our variables defined, we utilized MATLAB software to yield the vector *A*, the intensity effect of MPG-only data, by first creating a 2-D, 1181×1181 autocorrelation matrix, *R* (for *x*, i.e., G0 only data) using circular shifting. Next, a 1-D, cross-correlation vector, R_0 (between x and $\check{s}$, i.e., G0 only and MPG+G0 data), was created and applied to Eq. 3 to yield the vector *A* data (i.e., the intensity effect of the MPG only) [23]. Lastly, the resultant data was smoothed by a convolution kernel window equivalent to 15 pixels, or around $60\mu m$ to remove and minimize any noise present in the data.

3.2. Experiment at PBRC & Data Analysis

3.2.1. Experimental – Keck x-ray tomography machine

In the set of experiments conducted at PBRC, our proposed MCMS-MPG system was tested using 45kV x-rays with a 55uA current from a Hamamatsu Photonics K.K. unit the Keck x-ray tomography machine, seen in Figure 3.6 (a). These x-rays were detected on a Dexela 1512 GigE x-ray detector also seen in Figure 3.6 (a-c), as well as seen in Figure 3.6 (b), along with its spatial relation to the approximate locations of the source and grating positions. Figure 3.6(a) shows the system as looking down the beamline along the z-axis beginning with the x-ray source, down to the detector.

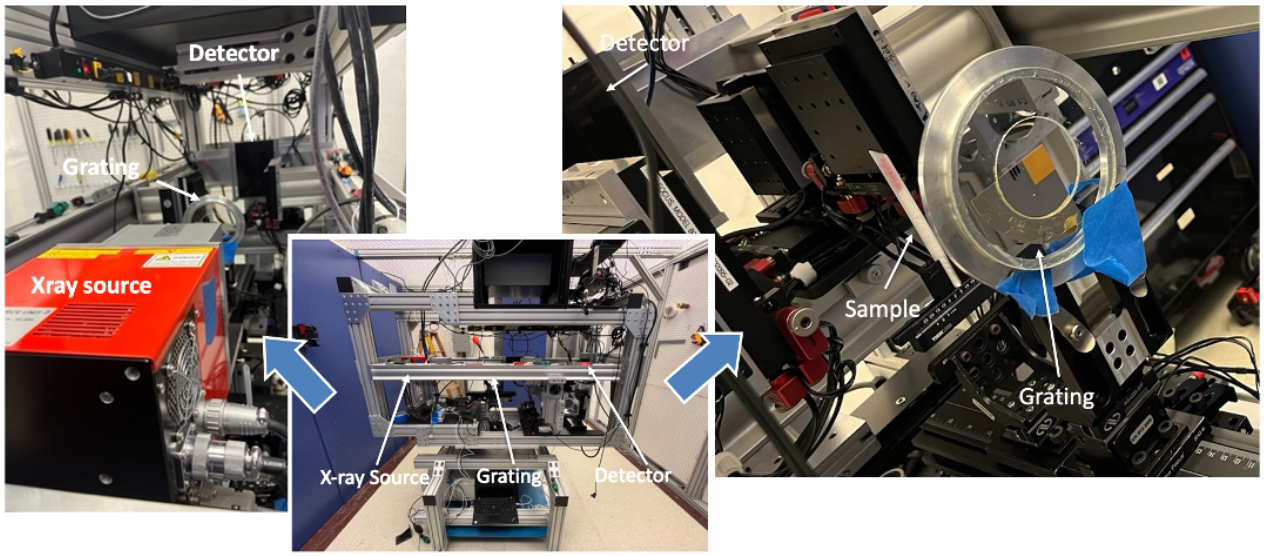

H. Meyer, J. Dey, S. Carr [24]

Figure 3.6. (A) View down x-ray beamline from source point-of-view. (B) Side view of Keck x-ray tomography machine. (C) Zoomed view of MPG and sample set-up.

For our G1 grating, we used two different types of modulated phase gratings for the imaging experiments at PBRC. The first was a rectangular MPG, designated MPG7, where the *h2* and *h1* are such that at 25 keV, the phase shifts are approximately $\frac{\pi}{2}$ and $\frac{\pi}{8}$ respectively, as seen in Figure 3.7(a). For the second type of MPG, we used a triangular MPG, designated TRMPG, where the *h2* and *h1* are such that at 25 keV, the peak phase shifts are approximately π and $\frac{\pi}{4}$ respectively, as seen in Figure 3.8 (a). In Figure 3.7(a) and Figure 3.8(a), a schematic drawing of the Keck experiment set-up is illustrated with both MPG7 and TRMPG in use, respectively. The total distance from the source to the detector was 110cm. The MPG to sample distance was 13.5cm and was kept at this constant distance of separation for each trial of exposures. The MPG to detector distance varied for the visibility experiments. The variable "*p*" is representative for the pitch of the specific MPG, the variable "F_p", representing the period of

the fringe pattern produced, and the variable "*W*", representing the period of the MPG with *h2* and *h1* specifying the phase modulation of the gratings.

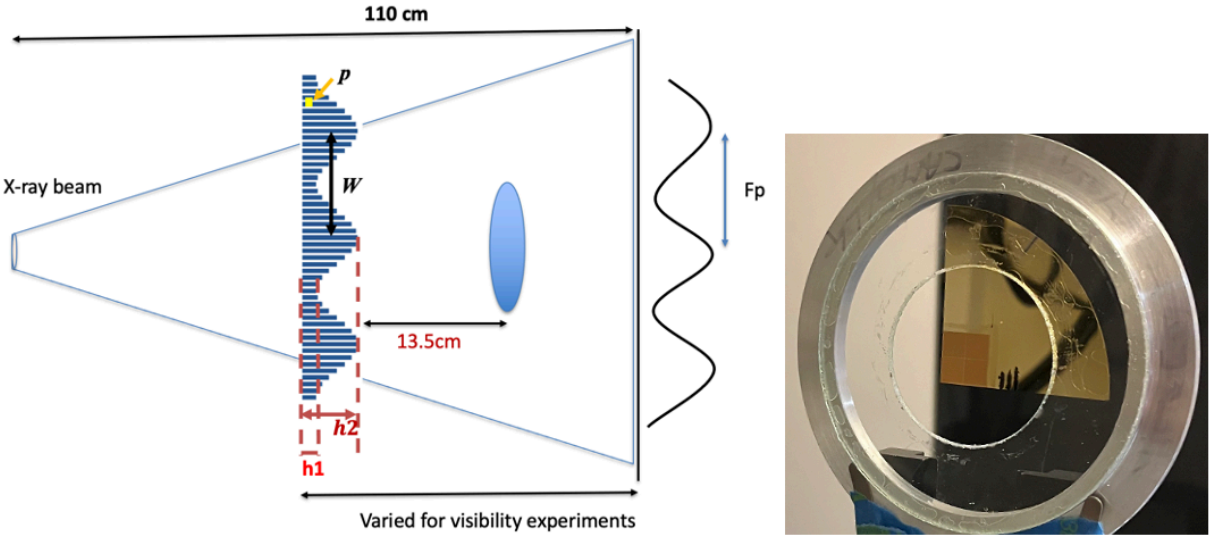

H. Meyer, J. Dey, S. Carr [24]

Figure 3.8. (A) Schematic of PBRC experiment set-up using TRMPG. (B) Zoomed view of triangular MPG, i.e., TRMPG.

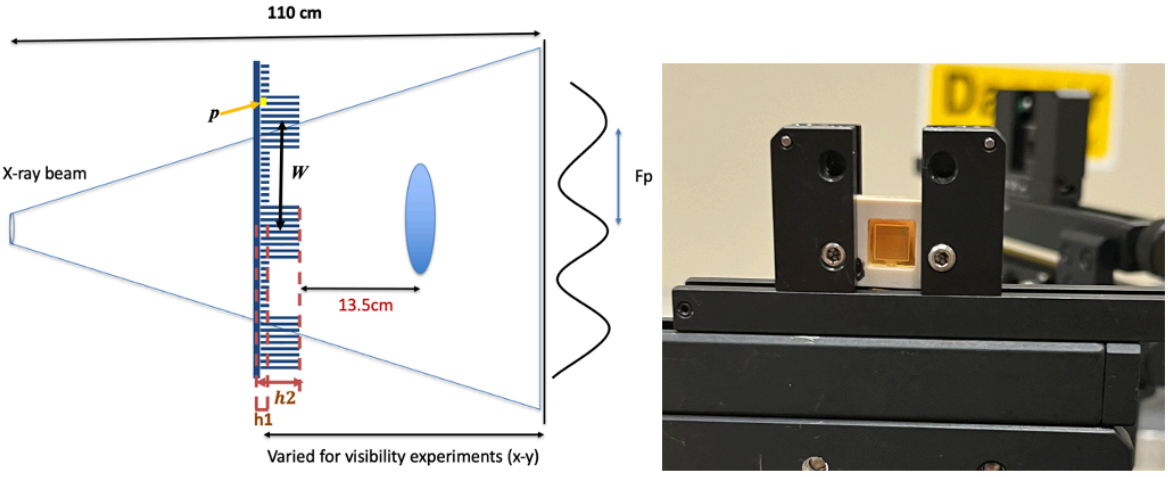

H. Meyer, J. Dey, S. Carr [24]

Figure 3.7. (A) Schematic of PBRC experiment set-up using MPG7. (B) Zoomed view of rectangular MPG, i.e., MPG7.

We decided to use a variety of samples for the experiments at PBRC in order to adequately supply us with images that will test the visibility of this system for a range of tissue types. First, we used a sample of an anchovy fish head, a sample of both boney and soft tissue to image. Next, we used a chicken bone, a sample of solely just boney tissue. Lastly, we used multiple asparagus seeds, a sample of more uniform composition. All the samples used are shown in Figure 3.9.

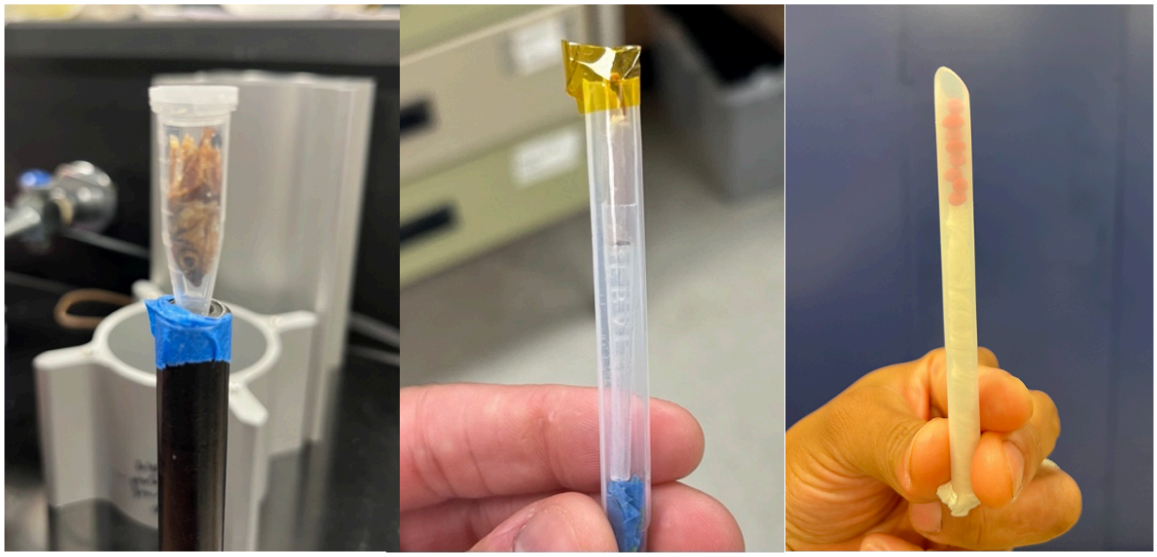

H. Meyer, J. Dey, S. Carr [24]

Figure 3.9. (A) Anchovy head. (B) Chicken bone. (C) Asparagus seeds.

3.2.2. Data Analysis – Marathe Method

Our interferometric data sets can be defined as a set of x-ray counts, c_{gp}, where $g = 1, \dots, M$ is the index that identifies each exposure, with one exposure at each grating displacement, and $p = 1, \dots, N$ is the index that identifies the "*pth*" pixel ($N \approx millions$) [26]. For our experiments at PBRC on the Keck machine, we took exposures for 7 different grating steps, x_g, therefore $g = 1, \dots, 7$. We then fit each set of exposures pixel by pixel to each pixel's

expected dependence on the grating position, followed by adapting a fitting algorithm that will ultimately transform this fitting operation into a simple matrix problem [26].

It is defined, that a grating-based phase-stepping interferometry data set consists of a set of pixelated images acquired as a function of grating stepping [26]:

$$\hat{c}_{gp} = a_{1p} + a_p \sin\left(\frac{2\pi}{p_{grat}} x_g + \phi_p\right) \tag{4}$$

Here, the amplitude of the interference term for the "*pth*" pixel is represented by a_p, the phase of the interference term for the "*pth*" pixel represented by ϕ_p and the period of the translated grating represented by p_{grat} [26]. After applying trigonometry, we can easily expand $\hat{c}_{gp}$ to the following equation:

$$\hat{c}_{gp} = \boxed{\mathbf{1}} a_{1p} + a_p \boxed{\sin\left(\frac{2\pi}{p_{grat}} x_g\right)} \cos(\phi_p) + a_p \boxed{\cos\left(\frac{2\pi}{p_{grat}} x_g\right)} \sin(\phi_p) \tag{5}$$

The bolded, boxed-in terms, or the fitting functions, within Eq. 5 can now be used to represent an $M \times 3$ matrix defined as B, specifically for our data sets, a 7×3 matrix B.

$$\hat{c}_{gp} = \sum_{\mu=1}^{3} B_{g\mu} a_{\mu p} \tag{6}$$

In Eq. 6, $a_{\mu p}$ is defined as one of the elements in the $3 \times N$ matrix a, specifically for our data sets [26]. This matrix a is a matrix of amplitudes, or weights, of the three fitting functions for N number of pixels, constant, sine and cosine, as seen in Eq. 7 (Hence, this is what we are trying to solve for in the end) [26]:

$$a_{1p} \equiv a_{1p}\ ,\ a_{2p} \equiv a_p \cos(\phi_p)\ ,\ a_{3p} \equiv a_p \sin(\phi_p) \tag{7}$$

Now that the fitting problem is essentially converted into a matrix problem, we still need to minimize the noise, this by calculating the minimization of the deviation-squared, D_p. First, the best fit is chosen for the set of coefficients, $a_{\mu p}$, that will effectively minimize D_p for each pixel [26]:

$$D_p \equiv \sum_{g=1}^{M} (c_{gp} - \hat{c}_{gp})^2 \tag{8}$$

To minimize D_p, we must first calculate the derivatives of each D_p with respect to each component of the matrix a, set all the deviations equal to 0 and then solve all the resulting matrix equations [26]. Since we are seeking the closest alignment of the fit vector, $\hat{\mathrm{c}}_{\mathrm{g}}$, with the data vector, c_{g}, we set $\frac{\partial \mathrm{D}}{\partial \mathrm{a_v}} = 0$ for $\mathrm{v} = 1, \ \ldots, 3$ [26].

We can then solve for a_μ as $\bar{a}$ via a sequence of matrix operations,

$$(B^T \cdot B) \cdot \bar{a} = B^T \cdot \bar{c} \tag{9}$$

$$\bar{a} = \boldsymbol{G} \cdot \bar{c} \tag{10}$$

$$\boldsymbol{G} = (B^T \cdot B)^{-1} \cdot B^T \tag{11}$$

Note, a transpose operation needed to be performed because the matrix B is not a square matrix, but $(B^T \cdot B)$ is, therefore we were then able to take the inverse of this, as illustrated in the steps between Eq. 9 and Eq. 11.

Now, the optimization problem is reduced to a matrix problem of simply multiplying a $3 \times M$ fixed matrix G into the $M \times N$ data matrix $\bar{c}$, yielding the resultant $3 \times N$ coefficient matrix a, shown in Eq. 10 [26]. We were able to perform these matrix operations efficiently using MATLAB software. Once the polar coordinates, a_p and ϕ_p in Eq. 12, of matrix a were recovered, the equations defined for phase recovery (Eqs. 13-15) can now be satisfied:

$$a_p = \sqrt{a_{2p}^2 + a_{3p}^2}\,, \phi_p = \tan^{-1}(\frac{a_{3p}}{a_{2p}}) \tag{12}$$

$$transmission = \frac{a_{1p}(sample)}{a_{1p}(reference)} \tag{13}$$

$$differential\ phase\ contrast = \phi_p(sample) - \phi_p(reference) \tag{14}$$

$$darkfield = \frac{a_p(sample)/a_p(reference)}{a_{1p}(sample)/a_{1p}(reference)} \tag{15}$$

The visibility of the fringe patterns can be simply calculated based off the maximum and minimum intensity of the interference patterns, illustrated in Eq. 16 below. This was done at different grating to detector distances in order to find the optimal range of visibility for our proposed system.

$$visibility = \frac{I_{max} - I_{min}}{I_{max} + I_{min}} \tag{16}$$

Chapter 4. Results

4.1. CAMD

4.1.1. Deconvolution

After performing the IFFT of the FFT ratio, FFT(MPG+G0) by FFT(G0) for the G0 to MPG distances of 2cm, 10cm, and 15cm cases, we have essentially performed the deconvolution of the MPG+G0 and G0-only signals. The resultant MPG-only signals are shown in Figure 4.1(A-C). Analysis of all 3 graphs reveal that the distance from peak-to-peak, i.e., the period, W, of the MPG-only graphs, measures to be between 208 µm and 264 µm.

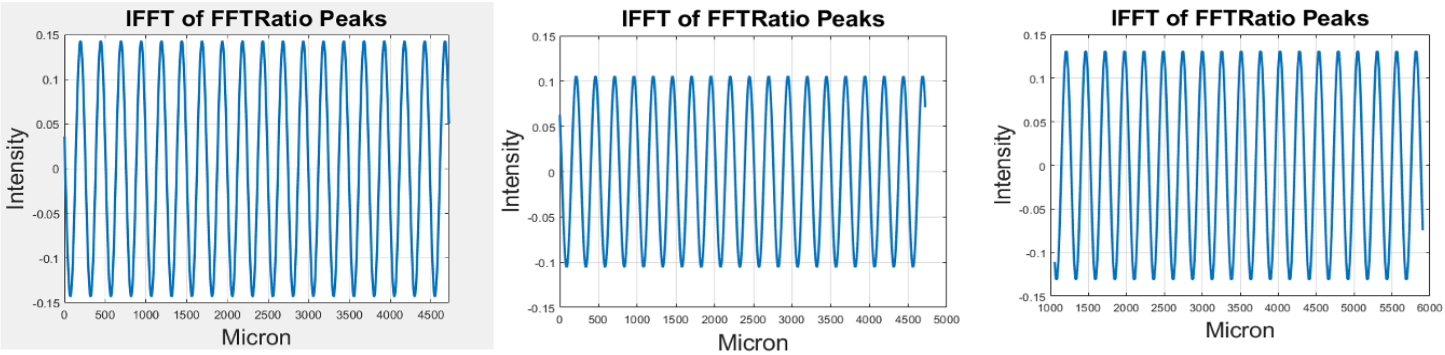

I. Hidrovo, S. Carr, et, al. [23]

Figure 4.1. (A) MPG-only signals recovered after deconvolution for G0-MPG distance equal to 2cm, (B) 10cm, (C) and 15cm.

4.1.2. Linear Optimization Estimation

The recovered intensity effect of MPG-only, I_{MPG}, computed by linear optimization minimizing sum-squared error before smoothing is shown below in Figure 4.2 and I_{MPG} after applying smoothing a smoothing kernel to reduce noise, shown in Figure 4.3. Analysis of the smoothed I_{MPG} signal shows that from peak-to-peak, i.e., the period, W, approximately measures between 208 µm and 264 µm as seen earlier in the results of the deconvolution method that was applied for the 3 different G0-MPG distances.

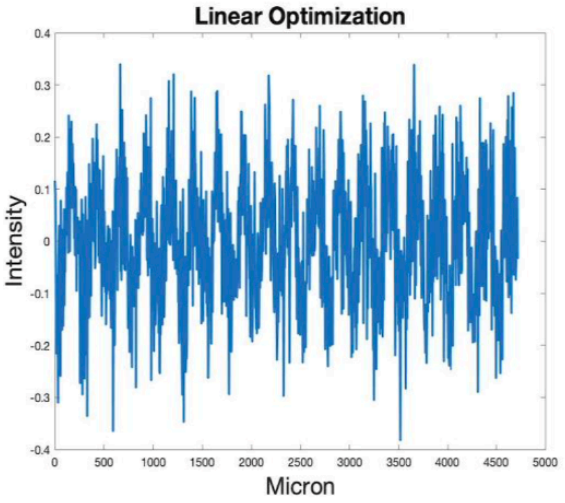

I. Hidrovo, S. Carr, et, al. [23]

Figure 4.2. Intensity effect of MPG-only minimizing sum-squared error before smoothing.

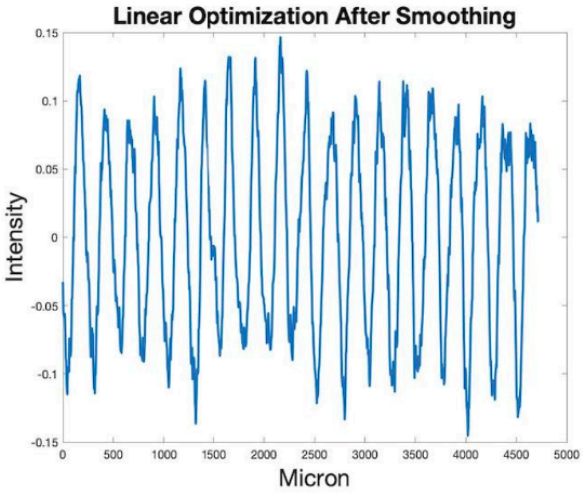

I. Hidrovo, S. Carr, et, al. [23]

Figure 4.3. Intensity effect of MPG-only minimizing sum-squared error after smoothing.

4.2. PBRC

4.2.1. Marathe Method

After the application of the Marathe Method to the resultant image data sets obtained from the PBRC experiments, we were able to generate plots detailing the visibility of both the MPG7 and TRMPG Q4 for our system set-up. The visibility plots for MPG7 and TRMPG are

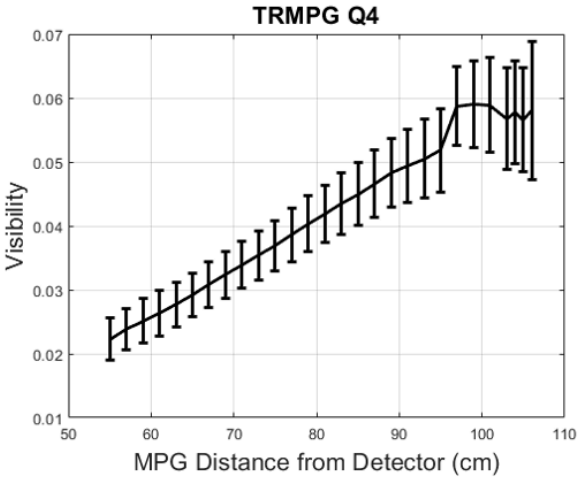

H. Meyer, J. Dey, S. Carr [24]

Figure 4.5. Resultant visibility plot for the triangular MPG, TRMPG.

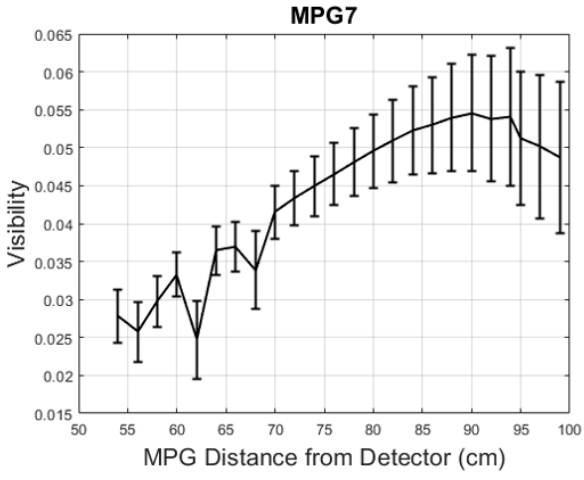

H. Meyer, J. Dey, S. Carr [24]

Figure 4.4. Resultant plot of visibility for the rectangular MPG, MPG7.

seen below in Figure 4.4 and 4.5, respectively.

For the MPG7 visibility plot, we can draw the conclusion that the peak visibility of our system set-up is when our MPG to detector distance falls between 87cm and 92cm. For the TRMPG Q4 visibility plot, we can see that the peak visibility will be when our MPG to detector distance falls between 98cm and 102cm.

4.2.2. Image Results from Samples

For the achovy head sample, we were able to recover both absorption and SAXS images, as seen in Figure 4.6(A-B) below. During this set-up, the TRMPG Q4 was used for imaging at a grating to detector distance of 81cm. In relation to the prior visibility plots produced using the Marathe Method, we marked where the visibility lies for a MPG-detector distance of 81cm on the plot and found it to lie right above 0.04 visibility.

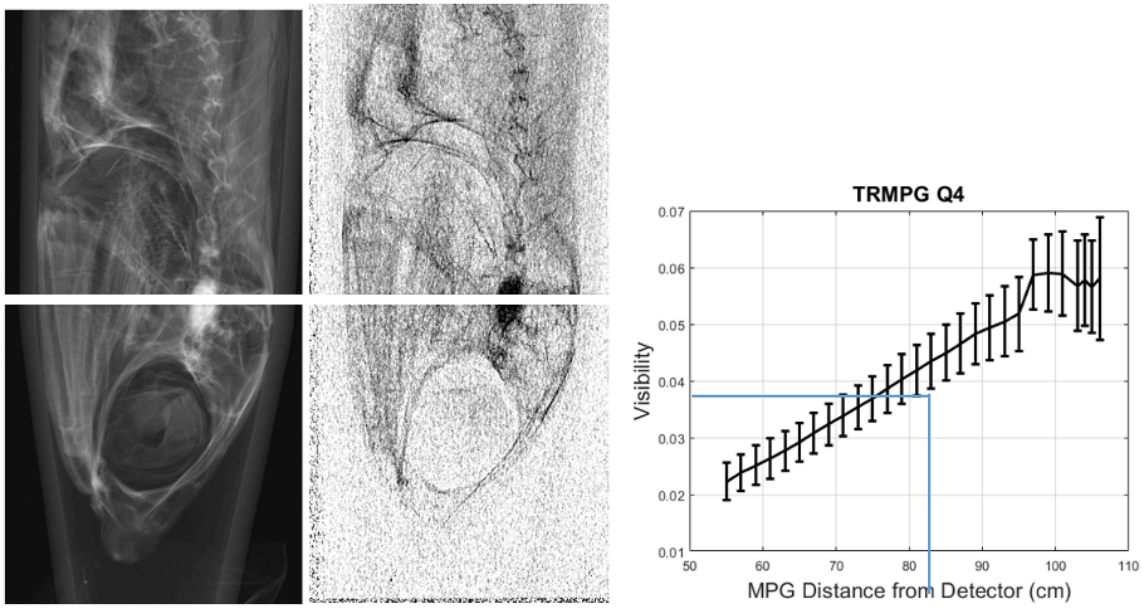

H. Meyer, J. Dey, S. Carr, et al

Figure 4.6. (A) Absorption (B) and SAXS, or dark-field, images for the Anchovy head sample using Q4 of the TRMPG. (C) TRMPG visibility plot marked with MPG-detector distance used, 81cm.

For the asparagus seeds sample, seen in Figure 4.7 (A-C), both absorption and SAXS images were recovered using the TRMPG Q4 identical to the anchovy head sample. Again, the MPG-detector distance used was 81cm, so this distance can be referenced back to the marked TRMPG visibility plot seen in Figure 4.6(C). Again, our visibility is equivalent to slightly more than 0.04 just like the anchovy head sample since the visibility of the system is dependent on the MPG-detector distance.

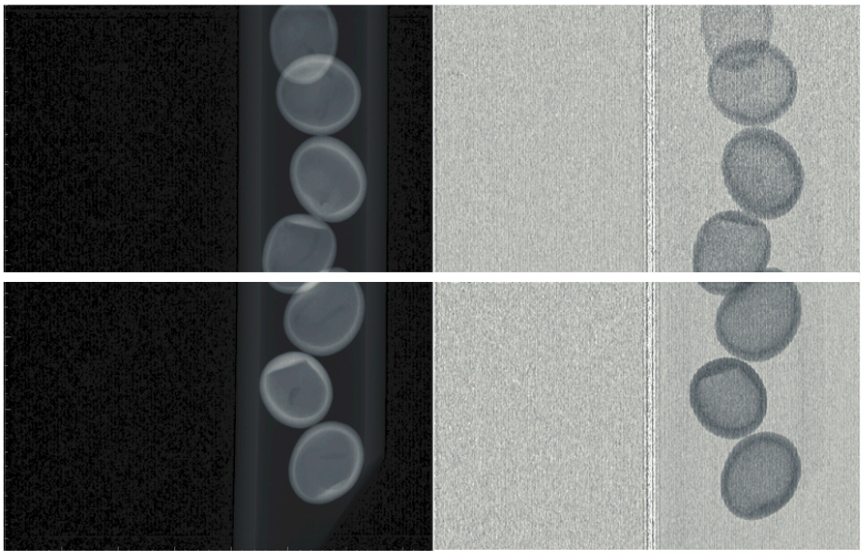

H. Meyer, J. Dey, S. Carr, et al [24]

Figure 4.7. (A) Absorption (B) and SAXS, or dark-field, images for the Asparagus seeds sample using Q4 of the TRMPG.

For the chicken bone samples, we recovered absorption, SAXS and differential-phase contrast images seen below in Figure 4.8(A-C). These images were produced using the MPG7 set-up with a grating-detector distances of 81cm, 80cm and 94cm for (A-C) respectively. We did so to again test the capabilities and extremes for our proposed MCMS-MPG system. Using the grating-detector distance information for each set of images, we marked on the MPG7 visibility plot to find the specific visibility for each of the distances, seen below in Figure 4.8(D).

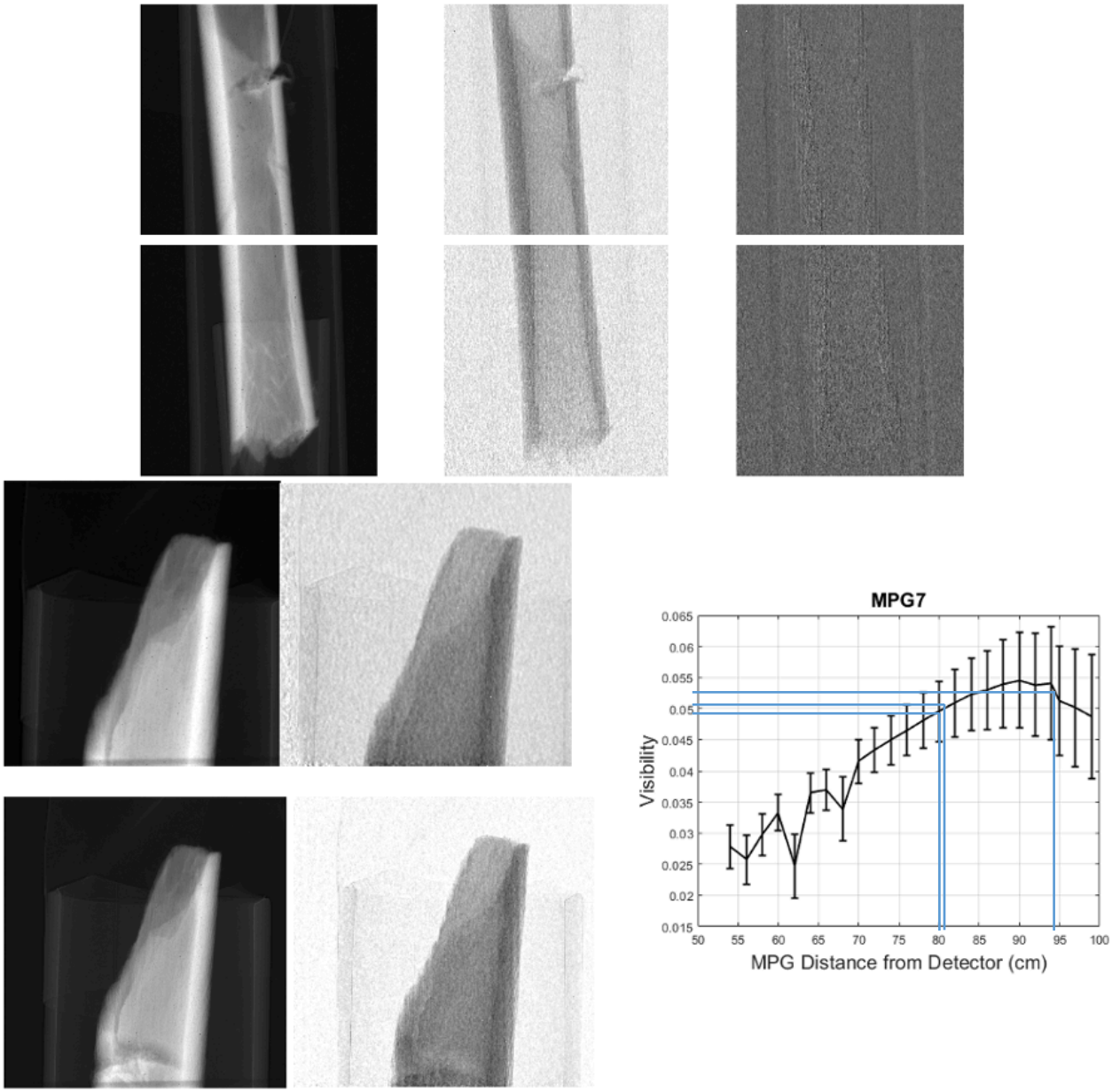

H. Meyer, J. Dey, S. Carr [24]

Figure 4.8. (A) Chicken bone sample imaged with MPG7 for grating-detector distance of 81cm, (B) 80cm, and (C) 94cm. (D) MPG7 visibility plot with relevantly marked MPG-detector distances.

Note: From left to right, the leftmost images for Figure 1.19(A-C) are absorption images, followed by SAXS images and then a single DPC image displayed in Figure 1.19(A).

Chapter 5. Conclusion and Future Work

5.1. Conclusion

5.1.1. CAMD

We were able to successfully remove the intensity effects from the G0 grating, obtaining just the intensity effect presumably due to the MPG alone. Consistent fringe patterns, again presumably due to the MPG alone. The observed, stable fringe patterns possessed measured periods from $208\mu m - 264\mu m$ for G0 to MPG distances 2cm, 10cm, 15cm. Both of our two independent methods of deconvolution and linear optimization estimation approximately matched with similar results.

5.1.2. PBRC

We were able to again view the fringe patterns presumably produced by the MPG alone. According to our visibility plots, we were able to draw the conclusion that the visibility increases as the MPG to detector distance increases as previously predicted by J. Xu, et al [22]. Our triangular MPG also yielded better results than the rectangular MPG.

5.2. Future Work

We seek to continue with imaging experiments for our proposed system by using actual breast tissue samples acquired from Woman's Hospital in Baton Rouge, LA. These samples will contain actual, malignant microcalcifications within them. This will provide us with yet another step towards our group's greater goal of making MPG clinically applicable and a reality for breast cancer screening.

Appendix A. Supplementary Information on Sensitivity and Specificity

According to the CDC, the analysis of sensitivity and specificity values for diagnostic imaging and other laboratory tests is used define clinical performance characteristics, aiding in selecting the most appropriate test for clinical needs [29]. The validity, or essentially the accuracy, of the test are defined by the sensitivity and specificity establishing a "gold standard" [27]. Different types of clinical tests will have different "golden standards" based on their sensitivity and specificity values [29]. Below are the equations for both sensitivity and specificity.

$$Sensitivity = \frac{(True\ Positive)}{(True\ Positive) + (False\ Negative)}$$

$$Specificity = \frac{(True\ Negative)}{(True\ Negative) + (False\ Positive)}$$

Appendix B. Marathe Method Expanded Derivation

It was initially explained that in order to recover the closest alignment of the fit vector, $\hat{c}_g$, to with the data vector, c_g, we must set $\frac{\partial D}{\partial a_v}$ equal to zero, expanded further and the equation rearranged accordingly. Eventually, we can solve for a_μ as $\bar{a}$ via a sequence of matrix operations, assuming for all pixels instead of just one like before. These calculations are shown below and shall flow starting from Eq. 10 in Chapter 3, section 3.2.2.

$$0 = \sum_{g=1}^{M} c_g B_{gv} - \sum_{g=1}^{M} \left(\sum_{\mu=1}^{3} B_{g\mu} a_\mu \right) B_{gv}$$

$$\sum_{g=1}^{M} \left(\sum_{\mu=1}^{3} B_{g\mu} a_\mu \right) B_{gv} = \sum_{g=1}^{M} c_g B_{gv}$$

$$\sum_{g=1}^{M} B_{vg}^T \left(\sum_{\mu=1}^{3} B_{g\mu 1} a_\mu \right) = \sum_{g=1}^{M} B_{vg}^T c_g$$

$$\sum_{\mu=1}^{3} \left(\sum_{g=1}^{M} B_{vg}^T B_{g\mu} \right) a_\mu = \sum_{g=1}^{M} B_{vg}^T c_g$$

$$\sum_{\mu=1}^{3} (B^T \cdot B)_{v\mu} a_\mu = (B^T \cdot \vec{c})_v$$

$$\left[(B^T \cdot B) \cdot \bar{a} \right]_v = (B^T \cdot \vec{c})_v$$

$$(B^T \cdot B) \cdot \bar{a} = B^T \cdot \bar{c}$$

$$\bar{a} = (B^T \cdot B)^{-1} \cdot B^T \cdot \bar{c}$$

$$0 = \sum_{g=1}^{M} c_g B_{gv} - \sum_{g=1}^{M} \hat{c}_g B_{gv}$$

For all pixels:

$$\bar{a} = G \cdot \bar{c}$$

$$G = (B^T \cdot B)^{-1} B^T \cdot \bar{c}$$

References

1. U.S. Department of Health and Human Services, Centers for Disease Control and prevention and National Cancer Institute; www.cdc.gov/cancer/dataviz, June 2018.

2. Desantis CE, Ma J, Sauer AG, Newman LA, Jemal A. Breast cancer statistics, 2017, racial disparity in mortality by state. CA: A Cancer Journal for Clinicians. 2017;67(6):439-448.

3. Howlader N, Noone AM, Krapcho M, Miller D, Bishop K, Kosary CL, Yu M, Ruhl J, Tatalovich Z, Mariotto A, Lewis DR, Chen HS, Feuer EJ, Cronin KA (eds). SEER

4. Cancer Statistics Review, 1975-2014, National Cancer Institute. Bethesda, MD, https://seer.cancer.gov/csr/1975_2014/, based on November 2016 SEER data submission, posted to the SEER web site, April 2017.

5. Siegel RL, Miller KD, Jemal A. Cancer statistics, 2018. *CA Cancer J Clin*. 2018; 68:7-30.

6. Jacobsen, KK., O'Meara, E.S, Dustin, K, Buist DSM, Kerlikowske, K Vejborg, I, Sprague, BL, Lynge, E, Euler-Chelpin, M, Comparing sensitivity and specificity of screening mammography in the United States and Denmark, *Int J Cancer*. 2015 Nov 1;137(9):2198-207. doi: 10.1002/ijc.29593. Epub 2015 Jun 1.

7. Vlahiotis A, Griffin B, Stavros AT, Margolis J, Analysis of utilization patterns and associated costs of the breast imaging and diagnostic procedures after screening mammography, *ClinicoEconomics and Outcomes Research*, vol. 10, 26 March 2018 Volume 2018:10 Pages 157—167

8. Chubak J, Boudreau DM, Fishman PA, Elmore JG, Cost of breast related care in the year following false positive screening mammograms, *Med Care*, 2010 Sep;48(9):815-20. doi: 10.1097/MLR.0b013e3181e57918.

9. Momose, A, et al, "Demonstration of X-ray Talbot-Lau Interferometry ", *Japanese Journal of Applied Physics,* vol. 42, Part 2, No. 7B, pp. L866-L868, July 2003

10. Momose A. Recent Advances in X-ray Phase Imaging. *Japanese Journal of Applied Physics*. 2005;44(9A):6355-6367.

11. Pfeiffer F, Weitkamp T, Bunk O, David C. Phase retrieval and differential phase-contrast imaging with low-brilliance X-ray sources. *Nature Physics*. 2006;2(4):258-261.

12. Weitkamp T, David C, Kottler C, Bunk O, Pfeiffer F. Tomography with grating interferometers at low-brilliance sources. *Developments in X-Ray Tomography V*. 2006.

13. Scherer K, Birnbacher L, Chabior M, Herzen J, Mayr D, Grandl S., Sztrókay-Gaul A, Hellerhoff K, Bamberg F, Pfeiffer F, "Bi-directional X-ray Phase-Contrast Mammography", PLoS ONE, vol. 9, no. 5, e93502, May 2014.

14. Grandl, S., Scherer, K. et al. Improved visualization of breast cancer features in multifocal carcinoma using phase-contrast and dark-field mammography – an ex- vivo study. *Eur. Radiol.* **25**, 3659–68 (2015)

15. Scherer KH. Screening Value of Phase-Contrast Mammography. *Springer Theses Grating-Based X-Ray Phase-Contrast Mammography*. 2016:59-75.

16. Wang Z, Hauser N, Singer G, Trippel M, Kubik-Huch RA, Schneider CW, Stampanoni M, "Non-invasive classification of micro-calcifications with Phase-Contrast X-ray Mammography", *Nature Communications* vol. 5, no. 3797, May 2014

17. Garrett J, Ge Y, Li K, Chen GH, Anatomical background noise power spectrum in differential phase contrast and dark field contrast mammograms, *Med. Phys.*, vol. 41, no. 12, pp. 120701-1-5, Dec 2014

18. Li K., Ge Y, Garret J, Bevins N, Zambelli J, Chen GH, Grating-based phase contrast tomosynthesis imaging: proof-of-concept experimental studies, *Med. Phys.*, vol. 41, no. 1, pp. 011903-1-11, Jan 2014

19. Dey J, Xu J, Ham K, Bhusal N, Singh V, "Novel Phase Contrast X-ray System", in *Proc IEEE NSS-MIC*, Oct 2017

20. Xu J, Dey J, Ham K, Bhusal N, Butler LG, "Two-dimensional Quadratic Grating for Far-Field Phase-Contrast X-ray Interferometry", in SPIE Proceedings10573: Physics of Medical Imaging; 1057323, SPIE Medical Imaging, 2018

21. US Patent Pending: J. Dey, N. Bhusal, L. Butler, K. Ham et. al., "Phase Contrast X-ray Interferometry", submitted July 2018

22. Xu J., Ham K., Dey J.,"X-ray interferometry without analyzer for breast CT application: a simulation study." J Med Imaging (Bellingham). 2020 Mar;7(2):023503. doi: 10.1117/1.JMI.7.2.023503. Epub 2020 Mar 26. PMID: 32258221; PMCID: PMC7096764

23. I. Hidrovo, S. Carr, K. Ham, L.G. Butler, A. Roy, J., Dey. "Observation of Fringe Patterns from a Modulated Phase Grating X-ray Interferometry System," Proc. SPIE vol. 12031, Medical Imaging 2022: Physics of Medical Imaging, 120313L (2022)

24. H. Meyer, J. Dey, S. Carr, K. Ham, L. Butler, I. Hidrovo, T. Varga, J. Schulz, T. Beckenbach, K. Kaiser, "X-ray Interferometry with a Modulated Phase Grating: Theory and Experiments" to be submitted *Nature Biomedical Engineering*, expected submission May 2023.

25. Papoulis, A. (1991) Probability, Random Variables, and Stochastic Processes. 3rd Edition, McGraw-Hill, New York.

26. Marathe S, Assoufid L, Xiao X, Ham K, Johnson WW, Butler LG. Improved algorithm for processing grating-based phase contrast interferometry image sets. Rev Sci Instrum. 2014

Jan;85(1):013704. doi: 10.1063/1.4861199. PMID: 24517772

27. Parikh R, Mathai A, Parikh S, Chandra Sekhar G, Thomas R. Understanding and using sensitivity, specificity and predictive values. Indian J Ophthalmol. 2008 Jan-Feb;56(1):45-50. doi: 10.4103/0301-4738.37595. PMID: 18158403; PMCID: PMC2636062.

28. IARC Working Group on the Evaluation of Cancer-Preventive Interventions. Breast cancer screening. Lyon (FR): International Agency for Research on Cancer; 2016. 2. Screening Techniques. Available from: https://www.ncbi.nlm.nih.gov/books/NBK546557/

29. Diagnostic Sensitivity and Specificity for Clinical Laboratory Testing. Center for Disease Control and Prevention Division of Laboratory Systems; 2022. https://www.cdc.gov/labtraining/docs/job_aids/additional_resources/Sensitivity_and_Specificity_Final_5_23_2022_508.pdf

30. American Joint Committee on Cancer. Breast. In: AJCC Cancer Staging Manual. 8th ed. New York, NY: Springer; 2017:589.

31. Berger M, Yang Q, Maier A. X-ray Imaging. 2018 Aug 3. In: Maier A, Steidl S, Christlein V, et al., editors. Medical Imaging Systems: An Introductory Guide [Internet]. Cham (CH): Springer; 2018. Chapter 7. Available from: https://www.ncbi.nlm.nih.gov/books/NBK546155/ doi: 10.1007/978-3-319-96520-8_7

32. Wang, Zhentian & Hauser, Nik & Singer, Gad & Trippel, Mafalda & Kubik-Huch, Rahel & Schneider, C. & Stampanoni, Marco. (2014). Non-invasive classification of microcalcifications with phase-contrast X-ray mammography. Nature communications. 5. 3797. 10.1038/ncomms4797.

33. F. Pfeiffer, J. Herzen, M. Willner, M. Chabior, S. Auweter, M. Reiser, and F. Bamberg, Z. Med. Phys. **23,** 176–85 (2013).

Vita

Sydney Carr was born in Houston, Texas in 1998. Sydney lived in Crosby, Texas on the outskirts of Houston attending Crosby High School where she further developed a deep love for physics and sports, graduating high school in 2016. Sydney enrolled at Houston Baptist University to pursue a Bachelor's degree in Physics while also competing in Division-1 Women's Basketball. After graduating from Houston Baptist University in 2020, she soon enrolled in LSU's Medical Physics Master of Science program. She plans to receive her Master of Science in Medical Physics in August of 2023. Following her graduation, Sydney plans to move back to her home state of Texas to begin a fulfilling career with Texas Oncology in Austin, TX.